EUMETSAT | **O3M SAF**

The EUMETSAT
Network of
Satellite
Application
Facilities

O3M SAF

Ozone and Atmospheric
Chemistry Monitoring

ALGORITHM THEORETICAL BASIS DOCUMENT

ATBD for the GOME-2 Aerosol products

Prepared by:

Martin de Graaf, Olaf Tuinder, Gijsbert Tilstra, Marloes Penning de Vries

Royal Netherlands Meteorological Institute

DOCUMENT STATUS SHEET

Issue	Date	Modified Items / Reason for Change
0.1	2006-11-15	First draft version
0.2	2007-06-06	Revisions after ORR-A2 comments.
0.3	2007-10-19	Revised after ORR-A2 review
0.4	2007-10-30	Revised after ORR-A2 CloseOut
0.6	2008-09-30	Revisions for ORR-B. Chap 4 inserted.
0.7	2009-04-15	Updated Chapter 4: retrieval implementation.
0.8	2009-09-01	Explicitly mentioned surface height in the algorithm description in section 3.3.4.4 and added ozone column and surface height to section 4.3. Algorithm version 0.6, Software version 1.20.
1.0	2010-04-29	Related to Software v1.22, Output Format v3.7; Update with Sun Glint Flag and Scattering Angle.
1.01	2010-05-25	Added info on O3MSAF
2.0	2012-03-13	Updated Chapters 3,4, and 6 to include SCI
2.1	2013-05-28	Added reference to PMD products. Small textual changes. Added description of degradation correction
2.2	2013-06-16	Changes based on ORR RIDs
2.3	2013-06-28	Revisions after ORR Review
2.32	2014-04-24	Typos fixed.
2.33	2014-11-12	Scope split. Heritage section added.

TABLE OF CONTENTS

1. INTRODUCTION

1.1 Purpose

This document is the Algorithm Theoretical Baseline Document for ARS, the GOME-2 aerosol product, which is part of the O3MSAF. This document presents the scientific background of the algorithm, presents an outline of its implementation and assists the user of this product in its physical interpretation. The document also presents a sensitivity study.

1.2 Scope

This ATBD provides information on the AAI and SCI parts of the ARS product.

1.3 Heritage

This algorithm was developed at KNMI in the PhD thesis work of Martin de Graaf and was implemented in the Opera software for ozone profile retrieval.

1.4 Glossary

1.4.1 Acronyms

AAI	Absorbing Aerosol Index
ARS	Aerosol Retrieval System
ATBD	Algorithm Theoretical Basis Document
B&P	Bass and Paur
CHEOPS	Climatology of Height-resolved Earth Ozone and Profiling Systems
DAK	Doubling-Adding KNMI
DFS	Degrees of Freedom for Signal
ECMWF	European Centre for Medium-range Weather Forecast
ERS	European Remote Sensing Satellite
ESA	European Space Agency
EUMETSAT	European Organisation for the Exploitation of Meteorological Satellites
FRESCO	Fast Retrieval Scheme for Cloud Observables
FWHM	Full Width Half Maximum
GDP	GOME Data Processor
GOME	Global Ozone Monitoring Instrument
KNMI	Royal Netherlands Meteorological Institute

LIDORT	LInearized Discrete Ordinate Radiative Transfer
LUT	Look Up Table
O3MSAF	Satellite Application Facility on Ozone and Atmospheric Chemistry Monitoring
OE	Optimal Estimation
OMI	Ozone Monitoring Instrument
OPERA	Ozone Profile Retrieval Algorithm
PMD	Polarization Measurement Device
PSC	Polar Stratospheric Clouds
RMS	Root Mean Square
RTM	Radiative Transfer Model
SAF	Satellite Application Facility
SAGE	Stratospheric Aerosol and Gas Experiment
SBUV	Solar Backscatter Ultra-Violet radiometer
SCI	SCattering Index
SZA	Solar Zenith Angle
TOMS	Total Ozone Mapping Spectrometer
UV	Ultra Violet
VIS	Visible

1.5 Reference documents

[RD1] De Graaf, M., P. Stammes, O. Torres, and R. B. A. Koelemeijer (2005), Absorbing Aerosol Index: Sensitivity analysis, application to GOME and comparison with TOMS, J. Geophys. Res., 110, D01201, doi:10.1029/2004JD005178

[RD2] De Graaf, M., Remote sensing of UV-absorbing aerosols using space-borne spectrometers, Ph.D. thesis, Free University, Amsterdam, 2006

2. INTRODUCTION TO EUMETSAT SATELLITE APPLICATION FACILITY ON OZONE AND ATMOSPHERIC CHEMISTRY MONITORING (O3M SAF)

2.1 Background

The need for atmospheric chemistry monitoring was first realized when severe loss of stratospheric ozone was detected over the Polar Regions. At the same time, increased levels of ultraviolet radiation were observed.

Ultraviolet radiation is known to be dangerous to humans and animals (causing e.g. skin cancer, cataract, immune suppression) and having harmful effects on agriculture, forests and oceanic food chain. In addition, the global warming - besides affecting the atmospheric chemistry - also enhances the ozone depletion by cooling the stratosphere. Combined, these phenomena have immense effects on the whole planet. Therefore, monitoring the chemical composition of the atmosphere is a very important duty for EUMETSAT and the world-wide scientific community.

2.2 Objectives

The main objectives of the O3M SAF is to process, archive, validate and disseminate atmospheric composition products (O3, NO2, SO2, OClO, HCHO, BrO, H2O), aerosols and surface ultraviolet radiation utilising the satellites of EUMETSAT. The majority of the O3M SAF products are based on data from the GOME-2 spectrometer onboard MetOp-A satellite.

Another important task of the O3M SAF is the research and development in radiative transfer modelling and inversion methods for obtaining long-term, high-quality atmospheric composition products from the satellite measurements.

2.3 Product families

Near real-time Total Column (NTO)

O3, NO2, O3Tropo, NO2Tropo

Near real-time Ozone Profile (NOP)

Near real-time UV Index (NUV)

Offline Total Column (OTO)

O3, NO2, O3Tropo, NO2Tropo, SO2, BrO, H2O, HCHO, OClO

Offline Ozone Profile (OOP)

Offline Surface UV (OUV)

Aerosols (ARS)

2.4 Product timeliness and dissemination

Data products are divided in two categories depending on how quickly they are available to users:

Near real-time products are available in less than three hours after measurement. These products are disseminated via EUMETCast (NTO, NOP), GTS (NTO, NOP) or Internet (NUV).

Offline products are available in two weeks from the measurement and they are archived at the O3M SAF archives in Finnish Meteorological Institute (OOP, OUV, ARS) and German Aerospace Center (OTO).

Only products with "pre-operational" or "operational" status are disseminated. Up-to-date status of the products and ordering info is available on the O3M SAF website.

2.5 Information

Information about the O3M SAF project, products and services: http://o3msaf.fmi.fi/

O3M SAF Helpdesk: o3msaf@fmi.fi

3. OVERVIEW

The Aerosol Index algorithm retrieves information on aerosols and clouds contained in the GOME UV/VIS Earthshine spectrum. In the next sections we will give a physical interpretation of the Aerosol Index and provide a theoretical sensitivity analysis.

The Aerosol Index consists of a signal contributed by aerosols that absorb UV/VIS radiation ("Absorbing Aerosol Index AAI") and by aerosols that absorb only little or no radiation ("SCattering Index SCI"). Due to their nature as indices in the UV/VIS wavelength range, the AAI is not sensitive to surface type and is defined in the presence of clouds – two cases where generic aerosol retrieval algorithms have problems. The aerosol types most clearly seen with AAI are desert dust, biomass burning aerosols, and volcanic ash; non-absorbing types such as secondary organic aerosols or sulphate aerosols can also be observed regularly with SCI. In the O3MSAF ARS product, the AAI from the Main Science Channels is derived from reflectances measured by GOME-2 at 340 and 380 nm. The AAI product from the PMDs is derived from the PMD bands closest to this wavelength pair. The actual wavelength values used are given in the output product. Note that the SCI is currently **not** produced by the O3MSAF.

The following products are produced:

Channel	Products
Main Science Channels	AAI at 40 x 80 km (340 / 380 nm)
Polarisation Measurement Devices	AAI at 40 x 10 km (338 / 381 nm)

4. ALGORITHM BACKGROUND

4.1 GOME Absorbing Aerosol Index

The Absorbing Aerosol Index indicates the presence of aerosols in the atmosphere. It separates the spectral contrast at two ultraviolet (UV) wavelengths caused by aerosol scattering and absorption from that of other effects, including molecular Rayleigh scattering, surface reflection, and gaseous absorption (Torres et al., 1998).

Traditionally, aerosol optical thickness measurements are being made using satellite-borne sensors operating in the visible (VIS) and infrared (IR) spectral range, where multiple scattering in the atmosphere is less important than in the ultraviolet (UV) and inversion calculations are relatively simple. In the VIS and near-IR range the large surface albedo of many land types makes retrieval of aerosols difficult over these regions. With the ongoing development of numerical radiative transfer codes and increasing computational speeds accounting for multiple scattering is no longer a problem, allowing for new techniques of aerosol measurements in the UV. Because the surface albedo of both land and ocean are generally small in the UV, this wavelength range is very suitable for aerosol detection.

We will adopt here the name residue (r) for the result of equation (1) in section 4.2.1, which is a quantity derived from measured reflectances. The name AAI is traditionally used to indicate absorbing aerosols, for which the residue has positive values; the name SCI was recently coined to include non-absorbing ("scattering") aerosols and clouds, which cause the residue to become negative. In the GOME-2 ARS product we will refer to the joint product of AAI and SCI as the residue (see also section 4.4).

The residue emerged as an error estimate in the Total Ozone Mapping Spectrometer (TOMS) ozone retrieval algorithm (Torres et al., 1998, 1999). As TOMS instruments have flown on various platforms from 1978 to 2006 providing nearly daily global coverage, the TOMS AAI record is the longest aerosol record available and it is used extensively to investigate aerosol impact on climate and study heavy dust, biomass burning and volcanic eruption events (e.g.: Hsu et al., 1996, Herman et al., 1997, Seftor et al., 1997, Chiapello et al., 1999, Pandi et al., 2001, Alpert et al., 2001, Moulin et al., 2004).

In this document we will give a physical interpretation of the Absorbing Aerosol Index and the SCattering Index , facilitated by presenting an analysis of the main sensitivities of the index. A theoretical basis for the AAI was given by Torres et al. (1998), using aerosol models with spectrally independent refractive indices. The radiance changes for different surface albedo, aerosol refractive indices, aerosol layer height and solar zenith angles were discussed, giving insight in the behaviour of an aerosol laden atmosphere and the resulting residue values therein. The main sensitivities were known qualitatively since 1997-1998: the residue is dependent on aerosol type (Torres et al., 1998) and on aerosol single

scattering albedo and aerosol layer height (Herman et al., 1997). The quantitative sensitivities have been investigated fully in [RD1] and [RD2], and are presented here.

Recently, new evidence showed the incorrectness of the assumption of a spectrally independent refractive index for mineral dust and the implications for the AAI (Sinyuk et al., 2003, Mahowald et al., 2004). The sensitivity of the residue for spectrally dependent refractive indices is compared to the residues found for spectrally independent refractive indices. The definition of the residue is given in section 4.2.1 and the calculation method used in this paper is presented in section 4.2.2. In section 4.3 the influence on the residue of aerosol micro- and macro-physical parameters, atmospheric optical, physical and chemical parameters and surface parameters are given separately, by means of a radiative transfer model study.

4.2 Residue Method

In this section, the definition and derivation of the residue is given and the method of calculation used for the GOME-2 data.

4.2.1 Definition of the Residue

The residue r is a wavelength-dependent variable defined as (Herman (1997))

$$r_\lambda = -100 \cdot \left\{ {}^{10}\log\left(\frac{I_\lambda}{I_{\lambda 0}}\right)^{meas} - {}^{10}\log\left(\frac{I_\lambda}{I_{\lambda 0}}\right)^{Ray} \right\} \qquad (1)$$

where I_λ is the radiance at the top of the atmosphere (TOA) at a wavelength λ.

The superscript I^{meas} refers to a measured TOA radiance of a real atmosphere with aerosols, as opposed to a calculated TOA radiance for an aerosol-free atmosphere with only Rayleigh scattering and absorption by molecules and surface reflection and absorption. The latter is referred to as I^{Ray}.

The reflectance is defined as

$$R = \frac{\pi I}{\mu_0 E_0} \qquad (2)$$

where E_0 is the solar irradiance at TOA perpendicular to the direction of the incident sunlight and μ_0 is the cosine of the solar zenith angle ϑ_0. So $\mu_0 E_0$ is the solar irradiance at TOA incident on a horizontal surface unit. Using equation (2) we can replace all quotients of radiances in equation (1) with quotients of reflectances.

If the surface albedo A_s for the Rayleigh atmosphere calculation is chosen so that

$$R_{\lambda 0}^{meas} = R_{\lambda 0}^{Ray}(A_s)$$
(3)

where λ_0 is a reference wavelength, equation (1) can be reduced to

$$r_\lambda = -100 \cdot {}^{10}\log\left(\frac{R_\lambda^{meas}}{R_\lambda^{Ray}}\right)$$
(4)

where $R_{\lambda 0}^{Ray}$ is calculated for surface albedo $A_s(\lambda_0)$, so the surface albedo is assumed to be constant in the range $[\lambda, \lambda_0]$. We will use for GOME-2 the wavelength pair λ/λ_0 : 340 nm/380 nm.

4.2.2 Calculation of the Residue

Equation (3) involves finding a surface albedo for which the measured reflectance at the reference wavelength is equal to the reflectance of a pure Rayleigh atmosphere with all scattering and absorption effects accounted for in the surface albedo. This inversion process was performed with Lookup Tables (LUTs) of the reflectances, as described below.

On the assumption that the atmosphere is bounded from below by a Lambertian surface, which reflects incident radiation uniformly and unpolarised in all directions, the surface contribution to the reflectance at TOA can be separated from that of the atmosphere (Chandrasekhar, 1960):

$$R(\mu, \mu_0, \phi - \phi_0, A_s) = R_0 + \frac{A_s t(\mu) t(\mu_0)}{1 - A_s s^*}$$
(5)

The first term, R_0, is the path reflectance, which is the atmospheric contribution to the reflectance. The second term is the contribution of the surface with an albedo A_s. t is the total atmospheric transmission, s^* is the spherical albedo of the atmosphere for illumination from below, μ is the cosine of the viewing zenith angle ϑ and $\phi - \phi_0$ is the relative azimuth angle.

The path reflectance can be expanded in a Fourier series. For a Rayleigh atmosphere the expansion is exact with only three terms in $\phi - \phi_0$, because of the cosine-squared scattering angle dependence:

$$R_0(\mu, \mu_0, \varphi - \varphi_0) = a_0 + \sum_{i=1}^{2} 2a_i(\mu, \mu_0) \cos i(\varphi - \varphi_0) \qquad (6)$$

R_0 is calculated with LUTs of $a_i(\mu, \mu_0)$, $t(\mu)$ and s^* for all wavelengths used. Then the surface albedo A_s in Equation (3) can be found from

$$A_s = \frac{R - R_0}{t(\mu)t(\mu_0) + S^*(R - R_0)} \qquad (7)$$

by replacing R by $R_{\lambda 0}^{meas}$ in equation (7). Note that this equation allows negative surface albedo, which occurs for highly absorbing (aerosol) layers.

Lookup tables of a_i, $t(\mu)$, and s^* were prepared as a function of μ an μ_0, surface pressure P_s and ozone column density Ω with the radiative transfer model DAK. The coefficients were calculated for 42 Gaussian distributed μ an μ_0 points, ozone columns of 167 and 501 DU and surface pressures of 1013, 802, and 554 hPa, as the dependence of the residue on total ozone column was found to be linear, whereas the dependence on surface pressure was non-linear. The surface albedo and reflectance were found by interpolation between these points. Interpolation between ground pressure points was performed with a second order polynomial, all other interpolations were linear.

The residue is calculated from the GOME-2 reflectances by taking 1-nm wide windows around 340 and 380 nm, in order to reduce the impact of small spectral shifts, Fraunhofer lines, etc.. The Rayleigh calculations are performed for exactly 340 and 380 nm.

4.3 Residue Sensitivities

The effects of several aerosol parameters on the residue were studied, as well as the effect of polarisation, clouds and atmospheric constituents, using the radiative transfer model DAK. Thereto the measured reflectances $R_\lambda / R_{\lambda 0}$ were replaced by simulated reflectances. The 340 nm/380 nm pair was chosen as the default pair.

4.3.1 Radiative Transfer Model DAK

The Rayleigh atmosphere reflectances and the LUT coefficients were calculated with the Doubling-Adding KNMI (DAK) radiative transfer model (Stammes, 2001). This model computes the monochromatic reflectance and transmittance in a plane-parallel atmosphere including polarisation, using the polarised doubling-adding method (De Haan et al., 1987). This method calculates the polarised internal radiation field of the atmosphere in an arbitrary number of layers, each of

which can have Rayleigh scattering, gas absorption, and aerosol and cloud particle scattering and absorption.

4.3.2 Standard Atmosphere, Geometry and Definition of Aerosol Models

For the atmospheric gas and temperature profile the standard Mid-Latitude Summer (MLS) atmosphere (Anderson, et al., 1986) was adopted throughout all calculations. The standard ground pressure was 1013 hPa, the standard ozone column was 334 DU. Linear polarisation was taken into account. A surface albedo of 0.05 was used to simulate dark surfaces and 0.6 to simulate bright surfaces. An aerosol layer could be introduced to simulate aerosol effects. The default altitude of the bottom of this one kilometre thick layer was three kilometres.

Two different types of phase functions were used to simulate the aerosols: the Henyey-Greenstein (HG) function and Mie phase functions. The HG phase function is defined as (Henyey (1941)):

$$\Phi(\cos\Theta) = \frac{1-g^2}{(1+g^2-2g\cos\Theta)^{3/2}} \quad . \tag{8}$$

Here Θ is the scattering angle and $g = <\cos\Theta>$ is the asymmetry parameter. The asymmetry parameter is a measure for the amount of forward scattered radiation by aerosols; the greater g, the greater the amount of radiation scattered in the forward direction. For Rayleigh scattering the amount of radiation in the forward direction is equal to the amount of backward scattering, so g is zero. The default value for the asymmetry parameter chosen for HG aerosol was $g = 0.7$, representing moderately forward scattering aerosols. The analytic HG function can be used to separate the effects of the single scattering albedo and the asymmetry parameter.

Table 1: Parameters for the aerosol models used in this study.

	λ	C2	D1a	D3	HG
r_g		0.14	0.12	0.50	-
v_g		1.45	2.20	2.20	-
Re(m)		1.55	1.55	1.55	-
Im(m)	340	0.04	0.0006	0.0006	-
Im(m)	380	0.04	0.0042	0.0042	-
ω_0	340	0.82	0.90	0.75	0.90
ω_0	380	0.83	0.93	0.81	0.90
g	340	0.73	0.70	0.83	0.70
g	380	0.73	0.69	0.80	0.70
τ	340	1.00	1.00	1.00	1.00
τ	380	1.04	1.01	1.01	1.00

Mie aerosol phase functions were used to model more realistic aerosols. In Mie calculations the complex refractive index m needs to be changed to vary the single scattering albedo, which also affects the asymmetry parameter. This introduces spectral variations in these parameters, which affect the residue calculations. Three types of aerosols were used, a carbonaceous aerosol model (C2), a small mode dust aerosol model (D1a) and a large mode dust aerosol model (D3). C2 is a smoke model with wavelength independent refractive index defined in Torres (1998), D1a is the fine dust model introduced in Torres (2002), with the updated imaginary part of the refractive index of Sinyuk (2003). D3 is the large mode dust aerosol model as defined by Torres (1998), also with the updated imaginary part of the refractive index of Sinyuk (2003). In Table 1 the values of the parameters of the different aerosol models used in this study are summarised. The size distribution of the Mie aerosols was assumed to be log-normal.

4.3.3 Sensitivity of the Residue for Mie Aerosol

Data on aerosol properties suggest that the refractive index of dust aerosol is strongly wavelength dependent in the UV (Patterson (1977), Sinyuk (2003)). This has implications for the residue, as will be shown below with the Mie aerosol models, in which this wavelength dependence is taken into account.
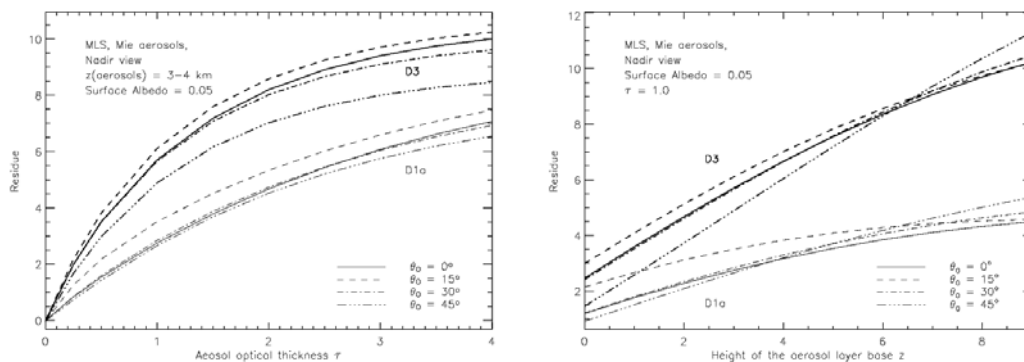
Figure 1: Mie aerosols: (a) Dependence of the residue on aerosol optical thickness. (b) Dependence of the residue on altitude of the aerosol layer z.

4.3.3.1 Aerosol optical thickness

Like with HG aerosol, the residue increases with aerosol optical thickness (Figure 1a). The increase is larger for larger aerosols, because the single scattering albedo is smaller (see Table 1). The residue is also much larger for aerosols with a wavelength dependent refractive index than for gray aerosols (cf. 1a); although the D1a aerosols have almost the same characteristics as the HG aerosols, they produce a much stronger residue increase for increasing aerosol optical thickness than the HG aerosols.

4.3.3.2 Aerosol layer altitude

The residue increases linearly with aerosol layer altitude, like it did for HG aerosol (cf. Figure 1b and 1b). The slope is proportional to the aerosol single scattering co-albedo, as was found in previous studies (Herman (1997), Torres (1998)). But there is an off-set for aerosols with a wavelength dependent refractive index: using gray aerosols the residue is positive only for aerosol higher than about one to two kilometres in altitude, whereas non-gray absorbing aerosols can be detected even very close to the surface.

This result is consistent with the study of (Mahowald (2004)), who found a stronger residue signal over mineral aerosol sources when gray dust aerosol models were replaced by aerosol models with wavelength dependent refractive indices. This implied the detection of non-gray aerosols closer to the surface, and thus closer to the source, than previously assumed.

4.3.3. Non-absorbing aerosols

The presence of small aerosol particles that do not absorb UV radiation leads to negative residues, of which the magnitude depends only on Aerosol Optical Thickness and its spectral dependence (which in turn depends on the size distribution of the particles) [Penning de Vries et al., 2009]. Non-absorbing aerosols can be of anthropogenic, volcanic (sulphate droplets), or biogenic (secondary organic aerosols) origin.

4.3.4 **Sensitivity of the Residue to Atmospheric, Surface and Geometric Parameters**
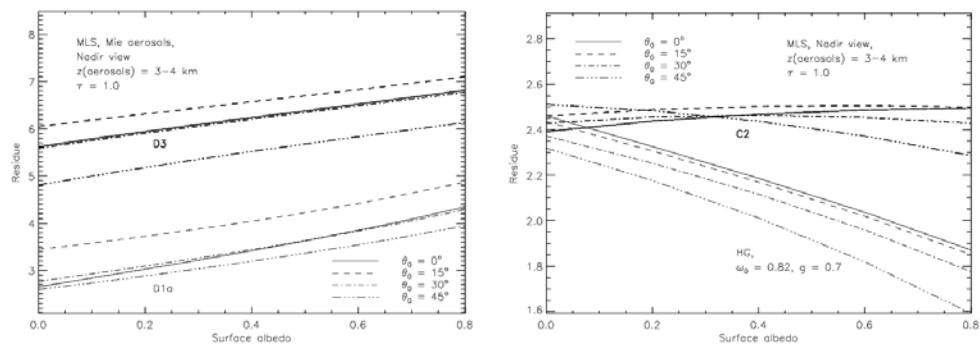
4.3.4.1 Surface albedo

Increasing the surface albedo has two competing effects. Firstly, it will increase the role of absorption by the aerosol layer compared to that of the surface. The reason is that below the aerosol layer radiation is bounced back and forth between the surface and the aerosol layer before escaping to space. Absorption takes place each time both at the surface and in the aerosol layer.

When the surface albedo is raised, the relative importance of the absorption by aerosols is increased, amplifying the effect of the absorption characteristics of the aerosol layer. This can be spectrally flat, producing no effect on the residue with increasing surface reflection, or wavelength dependent, increasing the residue with increasing surface reflection.

Secondly, increasing the surface albedo increases the amount of directly reflected radiation emerging at the top of the atmosphere, which results in itself in a zero residue. This will reduce the effect of an aerosol layer and lower the residue for increasing surface reflection.

Figure 2: Dependence of the residue on surface albedo for nadir view and solar zenith angles between 0° and 45°. (a) Atmosphere with Mie aerosols type D1a (normal lines) and D3 (bold lines). (b) Atmosphere with Mie aerosols type C2 (bold lines) and HG aerosols with C2 characteristics: τ =1.0, ω_0=0.82, g=0.7. (normal lines).

For aerosols of type D1a and D3, with strongly wavelength dependent single scattering albedo, the first effect is most important. So the residue increases for increasing surface reflection (Figure 2a).

For HG aerosols, with wavelength independent single scattering albedo, the first effect results in a constant residue for increasing surface albedo, but the second effect reduces the residue (Figure 2b). This is also true for a thin aerosol (gray or non-gray) layer; the presence of such a layer will only be felt when the amount of directly reflected radiation by the surface is small. On the other hand, the residue of a very thick layer of gray aerosols is constant with increasing surface albedo (not shown).

For smoke aerosols, like the C2 model with a weakly wavelength dependent single scattering albedo, the two effects balance each other and the residue does not change much with increasing surface albedo (Figure 2b).

The above result for gray absorbers can also be found in Torres (1998), where the residue versus aerosol optical thickness was modelled using gray absorbing and scattering aerosols over a dark (A_s =0.05) and a bright surface (A_s = 0.6). Using a bright surface instead of a dark surface hardly changed the residue for the absorbing aerosols (Figure 5 from Torres (1998)). The above result for the non-gray aerosols seems to be confirmed by observations. TOMS AAI values are

larger over underlying clouds, which serve as a bright surface. Smoke aerosols have been observed over both dark surfaces (e.g.: biomass burning aerosols over tropical forests in South America, Gleason et al., 1998) and over bright surfaces (e.g. biomass burning aerosols over snow and ice in Greenland, Hsu et al., 1999).
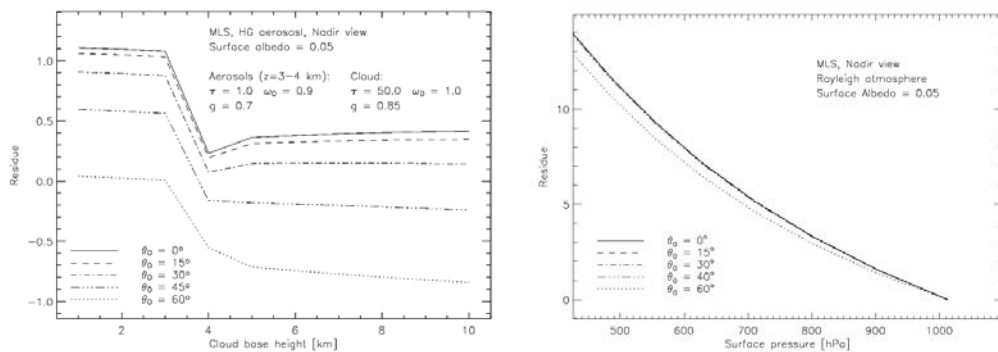
Figure 3: (a) Dependence of the residue on cloud base height, with an aerosol layer between 3 and 4 km altitude. The cloud has optical thickness τ = 50.0 and scattering particles with ω_0 = 1.0 and g=0.85. The base of the 1 km thick cloud was varied between 0 and 10 km in steps of 1 km. (b) Dependence of the residue on surface pressure. Rayleigh atmosphere with MLS profile, nadir view, solar zenith angles vary between 0° and 60° .

4.3.4.2 Clouds

The effect of clouds on the residue is comparable to the effect of a high surface albedo when the aerosols overlie the cloud. But when the cloud overlies the aerosols the residue is completely determined by the cloud characteristics. This is illustrated in Figure 3a with HG aerosols (the effect for Mie aerosols can be inferred from Figure 2). In Figure 3a a cloud was present at different altitudes in an atmosphere with an absorbing HG aerosol layer at an altitude of 3 -- 4 km. The cloud is modelled as scattering HG aerosols characterised by a high optical thickness of τ = 50, an asymmetry parameter g = 0.85 and a single scattering albedo ω_0 = 1.0. The vertical extent of the cloud is 1 km.

When the cloud is present under the aerosol layer (left side of Figure 3a) the residue is the same as for an aerosol layer over a bright surface. The cloud reflects almost all light incident on it, so effectively it becomes the new surface. As the cloud base is raised from 0 to 3 km the residue is slightly reduced due to a decrease in the amount of intercepted radiation by the aerosol layer (the distance between the cloud and the aerosol layer is reduced). Then there is a transition to a new situation when the cloud base is between 3 and 4 km and coincides with the aerosol layer. The residue drops by about 0.9. When the cloud base is raised even further the residue stays almost constant. The cloud intercepts almost all incident radiation and acts as an opaque 'roof' over the aerosol layer; consequently the residue is almost entirely determined by the cloud characteristics.

Aside from the increase in apparent surface albedo (for clouds below aerosols) and the shielding effect (for clouds above aerosols), clouds also have an own contribution to the residue, which depends on cloud optical thickness, cloud fraction, and measurement geometry [Penning de Vries and Wagner, 2011]. Clouds cause negative residues with a magnitude of up to -1.5 (for medium-sized clouds)..

4.3.4.3 Ozone absorption

A linear relationship between residue and ozone was found by scaling the total ozone column Ω (not shown). The reduction of the TOA reflectance due to ozone absorption is, to first order, equal to $\exp(-\tau_{O3}M)$, where τ_{O3} is the optical thickness of the ozone column and M is the geometrical air mass factor, $M = 1/\mu_0 + 1/\mu$. Since τ_{O3} is about 0.01 at 340 nm, the exponential can be approximated by $1 - \tau_{O3}$.

The dependence of the residue on Ω is limited: if Ω is increased from 100 to 500 DU, the 340nm/380nm residue increases linearly by 1. Therefore the ozone contribution in a Rayleigh atmosphere can be corrected for by linear interpolation. The LUTs include this dependence on Ω (see section 4.2.2).

Regarding the interaction of the absorption processes by ozone and aerosols, it has been shown that particle absorption effects introduce errors in the TOMS total ozone retrieval process, and a correction method making use of AAI has been developed (Torres (1999)).

4.3.4.4 Surface pressure / Surface height

The residue is strongly dependent on surface pressure (Figure 3b). The surface pressure was lowered by removing the lower part of a Rayleigh atmosphere, which also simulates the effect of topography. In this way an apparent residue is introduced, as a result of the reduced multiple scattering due to the lower amount of Rayleigh scatterers in the atmosphere. This effect is wavelength dependent, with more multiple scattering at lower wavelengths, yielding a residue. The dependence is not linear (Figure 3b), therefore the surface pressure is accounted for by a second order polynomial interpolation in the residue calculations (see section 4.2.2). We assume that the surface height and the surface pressure are linked via the hydrostatic equation.

4.3.4.5 Geometrical dependence

Since the residue is a radiance quantity, it not only depends on atmospheric and surface parameters, but also on solar and viewing geometry. This dependence is shown in [RD1]. The dependence on geometry is however, much less than on aerosol parameters, and is most strong for large solar and viewing zenith angles, and for azimuths in the principal plane.

4.3.4.6 Scattering Angle

The geometrical dependence is especially visible in areas where the total scattering angle is less than 90 degrees. In these areas there is much more forward scattering/reflection and the algorithm does not handle this well at the moment.

4.3.4.7 Sun Glint

The sea surface reflects sunlight like a mirror, and this increases the amount of light reaching up to the satellite. This mirror effect is not accounted for in the algorithm. Areas with risk of sun glint can be flagged, and some pixels can be permitted due to compensating or blocking effects of clouds. No sun glint is present over land. Two angles are used in the flagging procedure:

- Angle < 11 degrees; this is the 'core' angle and contains strongest reflectance.

- Angle < 18 degrees; this is the wider angle and sun glint in this area can be compensated / blocked by clouds with a cloud fraction larger than 0.3 or clouds with a cloud pressure lower than 850 hPa (cloud fraction must be larger than 0.1 in this case)

4.4 Defining the Absorbing Aerosol Index from the Residue

The above sensitivity study shows that there are at least two possibilities to create a positive residue. Firstly, an absorbing aerosol layer can absorb Rayleigh scattered radiation from below the layer. Because the Rayleigh optical thickness is strongly wavelength dependent this creates a difference in the reflectance at two UV wavelengths relative to that of a Rayleigh atmosphere, even with gray absorbers. When the absorbing ability of the layer increases more radiation is absorbed and the deviation increases, increasing the residue. The same is true when the amount of atmosphere under the absorbing layer increases.

Secondly, the aerosol absorption itself can be wavelength dependent, creating a spectral difference in the TOA reflected radiation. This will also create a positive residue if the absorption at the shorter wavelength is stronger, even when the aerosol layer is close to the surface. When the spectral absorption difference increases the residue will increase, meaning that different aerosol types produce different residues under the same circumstances.

The residue is not as sensitive to non-absorbing aerosols as to absorbing aerosols, yet such aerosols can clearly be identified in certain regions and seasons (e.g., south-eastern coast of U.S.A. in summer, or over Southeast Asia in August-September).

Often the residue is given only for cases where the residue is positive (Herman et al., 1997, Torres, 1998, De Graaf et al., 2005), excluding signals of clouds and scattering aerosols. Taken together, AAI and SCI offer are unique in allowing

distinguishing between absorbing and non-absorbing aerosols without *a priori* information on aerosol type. For this reason, both negative and positive residues are given in the ARS data product.

The calculation of the residue often involves using negative surface albedo and its absolute value has no unique interpretation, but high values of the AAI indicates the presence of absorbing aerosol layers, both over dark and bright surfaces. There have been some efforts of translating the AAI into physical meaningful parameters (Gleason (1998), Hsu (1999)), but we prefer to present the AAI itself rather than a derived product, because the interpretation of the AAI is still developing.

[RD1] shows that the AAI from GOME-1 corresponds well to occurrences of biomass burning and dust events, which are major sources of absorbing aerosols.

The residue is also sensitive to sun glint, which scenes should be flagged. Sun glint is expected in GOME-2 data at the east side of the swath.

The residue is very sensitive to the absolute radiometric calibration of satellite reflectances at 340 and 380 nm: 1 residue unit is equal to 2.3 % reflectance change; a change of 0.1 residue units is well detectable by GOME-1, i.e. a change of 0.2 % in reflectance ([RD1]). Recently, the residue has been found to provide also interesting information on calibration degradation of SCIAMACHY ([Tilstra et al., 2012a]).

5. RETRIEVAL IMPLEMENTATION

5.1 Framework

The Absorbing Aerosol Index algorithm re-uses a lot of code from the general framework of the Opera Ozone Profile Retrieval Algorithm (see ATBD for the OOP product). The same Level-1B reading routines are used and a lot of the same internal structures. The implementation of the algorithm is divided into steps detailed below.

5.2 Initialisation

In the initialisation step the software reads a configuration file, a work order file and it reads the reference data. In the case of the Absorbing Aerosol Index algorithm the reference data consists of the Rayleigh look-up-tables for the wavelengths selected by the user in the configuration file. Additionally, ozone columns from an Assimilated Total Ozone (ATO) file are used as input. If no ATO is available, the total ozone column is extracted from an ozone profile climatology selected via the configuration file. Next, some basic structures for reading the Level-1B data are set up, as well as structures for internal data records.

5.3 Ingestion and Data Selection

In the ingestion step, the software reads a number of MDR Earthshine records from the Level-1B file. From these MDR records the necessary information for the Absorbing Aerosol Index algorithm is selected, and copied into an internal data structure: the 'AAI-Structure'. This AAI-Structure contains information on geolocation, date/time, solar and viewing angles, surface height, the ozone column (from ATO or climatology), and the reflectance around selected wavelengths, averaged with a triangular slit over a user defined width. The information is stored on a ground pixel granularity (size is following the Band-2b pixel size). Per ground pixel there is a flag indicating whether the information stored is valid.

5.4 Degradation Correction

The correction for instrument degradation described in this section is currently not applied to operational NRT and offline AAI products.

Instrument degradation is a serious problem which strongly affects the Earth reflectance measurements performed by GOME-2 in the UV wavelength range [Tilstra 2012b]. As a result, it also has an impact on the reflectances of the 340/380 nm wavelength pair used in the AAI retrieval algorithm. The method for in-flight degradation correction that we use has been introduced earlier in [Tilstra

2012a] for the SCIAMACHY instrument. The method was later applied to the GOME-2 instrument [Tilstra 2012b].

The method is based on studying time series of the daily global mean reflectance. The daily global mean reflectance, denoted by R*, is defined as the mean of all measured Earth reflectances for a certain scan mirror position on a certain day between 60ºN and 60ºS and solar zenith angles θ_0 less than 85 degrees. In *Figure 4* we present a plot which shows the daily global mean reflectance measured at 340 nm (green) and 380 nm (red) as a function of time for GOME-2 on MetOp-A.
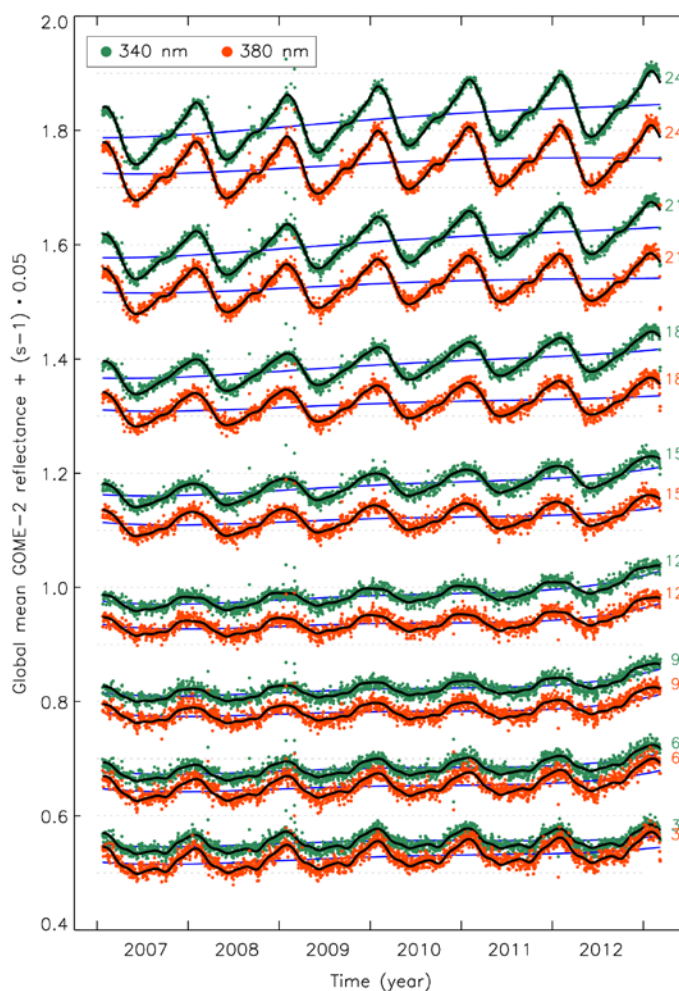
Figure 4: Global mean reflectance measured by GOME-2 at 340 nm (green) and 380 nm (red) as a function of time, for some of the 24 scan mirror positions in the forward scan. To separate the time series graphically, an offset of (s-1)·0.05 was added to each, where s is the scan mirror position as indicated. The solid black curves are fit results and are described in the main text. The blue monotonous curves illustrate the effect of instrument degradation on the reflectance over the years.

The time series of the global mean reflectance show seasonal variations as well as trends due to instrument degradation. To analyse the time series, we assume that the global mean reflectance may be well described empirically by a function made up of a polynomial term, representing the reflectance change due to instrument degradation, multiplied by a term periodic in time that represents the normal seasonal variation of the global mean reflectance. In other words,

$$R^{\star}_{\lambda,s} = P^{(p)}_{\lambda,s} \cdot \left[1 + F^{(q)}_{\lambda,s}\right] , \tag{9}$$

where the term P represents the polynomial part of degree p, defined by

$$P^{(p)}_{\lambda,s}(t) = \sum_{m=0}^{p} u^{(m)}_{\lambda,s} \cdot t^{m} , \tag{10}$$

while the seasonal variation F is described by a finite Fourier series of order q, according to

$$F^{(q)}_{\lambda,s}(t) = \sum_{n=1}^{q} \left[v^{(n)}_{\lambda,s} \cdot \cos(2\pi n t) + w^{(n)}_{\lambda,s} \cdot \sin(2\pi n t) \right] . \tag{11}$$

In these equations, the parameter t is the time expressed in years since the beginning of the time series. The parameter λ refers to the wavelength studied and the integer s relates to the scan mirror position. For the main science channel (MSC) spectral measurements of GOME-2, this integer runs from 1 to 32 for the nominal integration time (IT) of 187.5 ms when the instrument scans from east to west and back. For the PMD measurements, the parameter s runs from 1 to 256. For the present baseline, we use p = 4 and q = 6.

The polynomial part P is the most important as it represents the relative change in the GOME-2 measured Earth reflectance over the years, per scan mirror position, due to instrument degradation. Normalisation of P immediately leads to the reflectance degradation factor:

$$d_{\lambda,s}(t) = P^{(p)}_{\lambda,s}(t) / P^{(p)}_{\lambda,s}(0) \tag{12}$$

For GOME-2 the reflectance degradation factor is growing with time for most wavelengths, and is strongly dependent on scan mirror position.

The correction for instrument degradation can easily be calculated using

$$c_{\lambda,s}(t) \equiv 1/d_{\lambda,s}(t) = P^{(p)}_{\lambda,s}(0) / P^{(p)}_{\lambda,s}(t) . \tag{13}$$

The measured Earth reflectances have to be multiplied with these correction factors. As mentioned before, the correction depends on wavelength, scan mirror position, and time.

5.5 Retrieval

The retrieval is done for pixels where the validity flag indicates valid spectral measurements and valid auxiliary data. The inputs for the retrieval are spectral measurements at two wavelengths, the surface height, the ozone column, and also the geometry (SZA, VZA and the Relative Azimuth Angle).

The lookup tables contain reflectances at the two chosen wavelengths, as well as the s*, and t. The parameter t is the total atmospheric transmission for the given zenith angle, s* is the spherical albedo of the atmosphere for illumination from below. The lookup tables were created using the radiative transfer code DAK (which stands for Doubling-Adding KNMI). This vector RTM takes polarisation into account, as well as ozone absorption and Lambertian surface reflection. Additionally, a pseudo-spherical description of the atmosphere was used and O2-O2 absorption was taken into account assuming a background level of oxygen. The dimensions of the lookup tables are: total ozone column, surface height, mu, and mu0.

The core of the retrieval computes the residue by cubic spline interpolation in mu and mu0 of path reflectance and analytically computed surface albedo. This is explained in the sections on algorithm description above.

At the end of the retrieval routine we perform a range check on the retrieved residue value, setting it to an error value if it is out of range.

5.6 Quality Flags

During the processing the software keeps track of a number of Quality Flags related to the input and the processing itself. Some flags are copied over from the L1b data. Some are set as a result of quality control of input data, some are set as a result of missing external data. The list below in Table 2 shows the origin of the quality flag or when certain flags are set. The flag sets are split in Quality Input and Quality Processing flags.

Table 2: List of input and processing quality flags.

QualityInputFlags	
DegradedInstrumentFlag	Non-nominal level 1 due to instrument degradation; Flag is copied over from L1b flag called DEGRADED_INST_MDR
DegradedProcessorFlag	Non-nominal level 1 due to processing degradation; Flag is copied over from L1b flag called DEGRADED_PROC_MDR
SouthAtlanticAnomalyFlag	Groundpixel is in SAA; F_SSA in Level1b/PCD_BASIC
RecentSunFileMissing	Sunfile of date missing: older sunfile used
EarthshineRadianceDataMissing	Earthshine Radiance data missing

EarthshineRadianceDataInvalid	Earthshine Radiance data invalid
SolarIrradianceDataMissing	Solar Irradiance data missing
SolarIrradianceDataInvalid	Solar Irradiance data invalid
AAIDataInvalid	Absorbing Aerosol Index input data invalid due to input errors ((ir-)radiance) or out of bound geometry conditions (Solar Zenith Angle, Solar Azimuth Angle, Viewing Zenith Angle, Viewing Azimuth Angle, Relative Azimuth Angle, ScatteringAngle) or external input valies like out of bound surface pressure or total ozone column)
FailureForwardInSetup	Failure in the set up of atmospheric profiles (e.g.: Pressure, Height, Temperature, Ozone)
SunGlint	Sun Glint flag
Other	Other error
QualityProcessingFlags	
NoRetrievalDone	Set when any kind of input error is detected.

5.7 Storage

Data from the AAI-Structure has the dimensions of the width of the MDR and the number of MDRs that were read in at one time. This AAI structure does not contain the full PDU worth of data. The AAI-Structure is sent to the output module where, together with Product Specific Metadata such as the selected wavelengths and the width of the triangular slit used in the selection of the reflectances, all relevant parameters are copied into an extensible data structure (geolocation, date/time, AAI).

5.8 Output

When the main program has signalled that no more input data was found (e.g.: at the end of a Level-1B file), an output file is produced that conforms to the O3MSAF format: Metadata, Product Specific Metadata, a Geolocation Group and a Data Group. Please refer to the Product User Manual for detailed information on format and content.

6. VERIFICATION OF THE GOME-2 AAI AND SCI PRODUCTS

6.1 Verification of AAI from the Main Science Channels

As a first verification of the GOME-2 AAI algorithm from the main science channels, we show in Fig. 4 a series of four days for which the GOME-2 AAI is compared globally to the OMI AAI, which has been taken from the OMI ozone product, processed according to the TOMS v8 algorithm (see ftp://toms.gsfc.nasa.gov).

The situation covers the period 20-23 June 2007, where a large Saharan desert dust cloud was transported westwards over the Atlantic Ocean (Fig. 4). Because the GOME-2 AAI map contains the entire range of the residue from -2.5 to 4.5, there are values for the entire globe. The OMI AAI map only contains the residue values above 1.0, so it selects absorbing aerosol scenes. It is clearly visible that the Saharan dust storm is picked up nicely in the GOME-2 AAI data. A plume of biomass burning aerosol west of the coast of southern Africa is seen in both GOME-2 and OMI data.
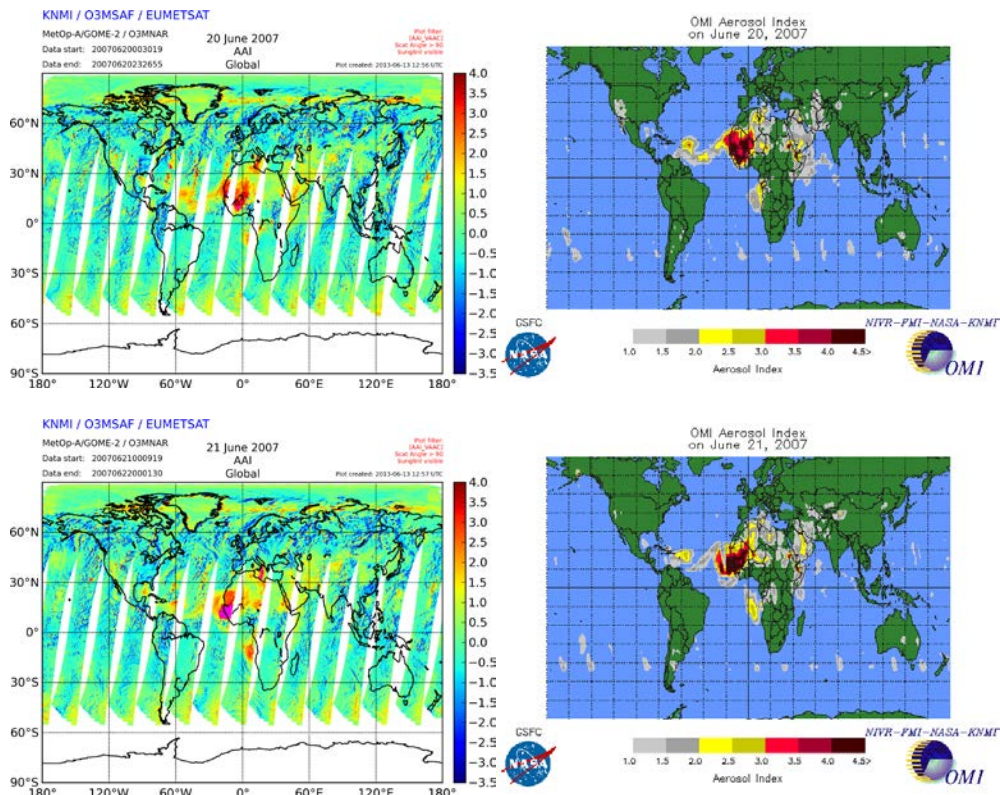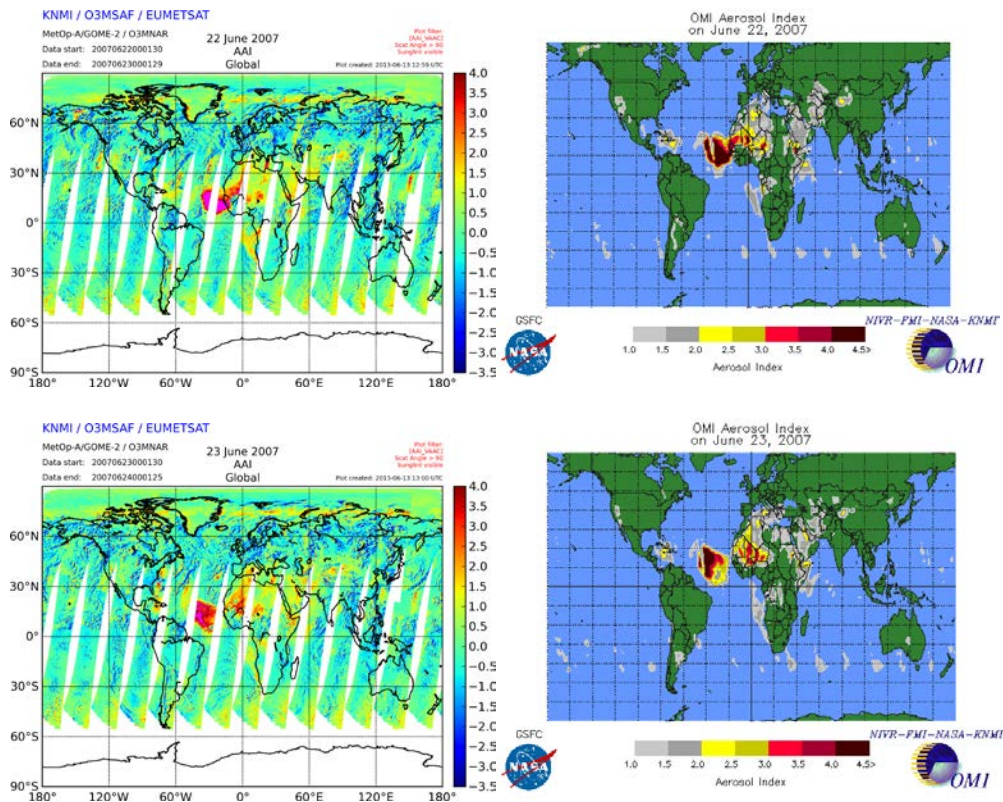
Figure 5: AAI from GOME-2 on Metop-A (left figures) and AAI from OMI (right figures) for the period June 20th-23rd 2007. Note the different AAI ranges and colour scales for GOME-2 and OMI.

## 6.2 Verification of SCI from the Main Science Channels

*Note that the SCI is currently **not** produced by the O3MSAF.*

For verification of the SCI, the colour scale is changed so that non-absorbing aerosols (yellow-red tones) are more easily observed. Absorbing aerosols appear in blue. In Figure 5, we show the average GOME-2 residue (right panel) and MODIS Aerosol Optical Thickness (at 550 nm, left panel) over North America in August, 2007. MODIS AOT clearly shows enhanced aerosol amounts over several regions during this month. These patterns are also seen in the residue, with additional information on aerosol absorption: for example, the aerosols in the left black box drawn in both panels (Southwest USA) cause positive residue (non-zero AAI) because they are mineral dust particles that absorb UV radiation. In contrast, the aerosols in the right black box (Southeast USA) are secondary organic aerosols that absorb little or no UV radiation and cause negative residues (non-zero SCI). Thus, the combination of AAI and SCI allows absorbing and non-absorbing aerosols to be distinguished at a glance.
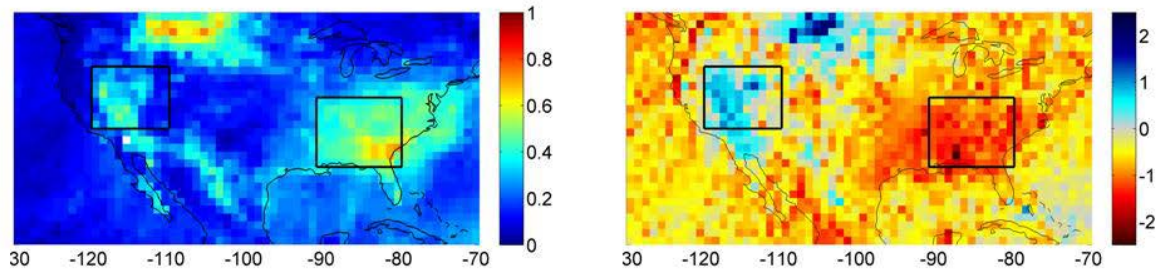
Figure 6: Monthly averaged Aerosol Optical Thickness from MODIS (left panel) and Absorbing Aerosol Index from GOME-2 (right panel) for August, 2007. No cloud filter was applied to the GOME-2 data. The boxes indicate the regions studied in detail in Figure 7.

A more quantitative comparison of AAI and SCI was performed for the two boxed regions in Figure 5. For each region, an average AOT and residue were computed for each month of the years 2007 and 2008. The time series depicted in Figure 6 show good qualitative agreement between MODIS AOT and GOME-2 residue, and it can be clearly seen that non-absorbing aerosols (seen in Southeast USA, panels A and B) cause a negative residue (non-zero SCI), whereas absorbing aerosols (in Southwest USA, panels C and D) cause positive residues (non-zero AAI). Monthly averages were also computed for GOME-2 residues with a cloud filter of CF<0.2 applied (dotted lines and circles in panels B and D), but this does not influence the results significantly. AAI and SCI thus allow the detection of aerosols even in the presence of clouds.
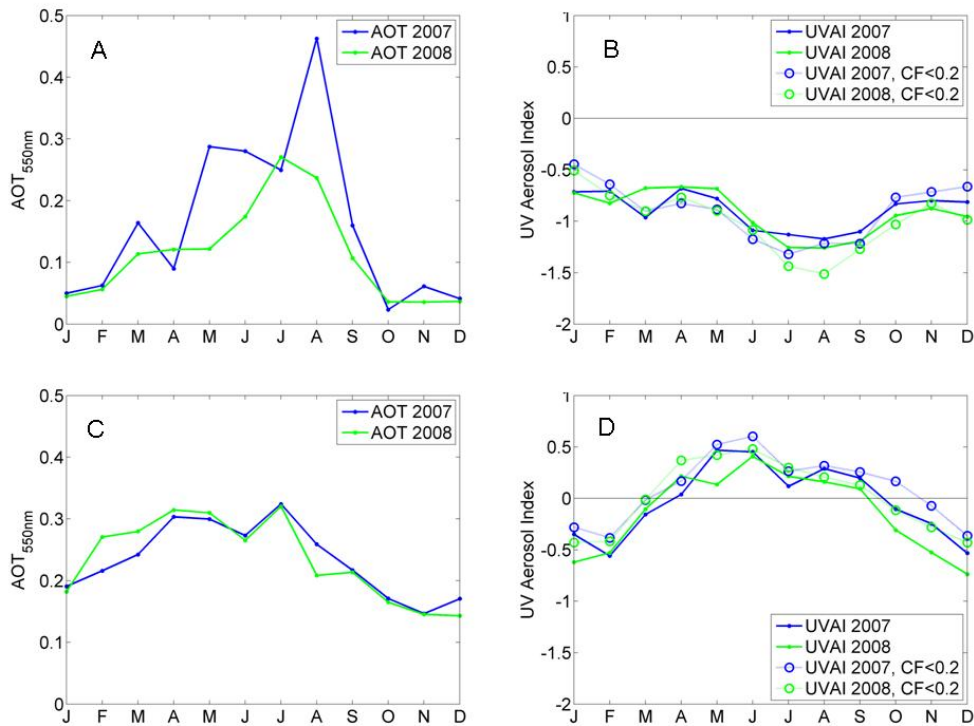
Figure 7: Time series of monthly averaged MODIS Aerosol Optical Thickness at 550 nm (panels A and C) and GOME-2 Absorbing Aerosol Index (B,D). The time series are shown for the boxes depicted in Figure 5: Southeast USA in panels A and B, and Southwest USA in panels C and D. Average residues were calculated without (dots, solid lines) and with a cloud filter (CF<0.2, circles and dotted lines).

6.3 Verification of the AAI from PMD

In Figure 8 we show a side-by-side comparison of the AAI from the PMD band versus the AAI from the Main Science Channels. On the left the MSC AAI is shown and on the right the AAI from the PMDs is shown. For this figure, data from Metop-B are used.

The plots show that the desert dust is located in the same locations in both the MSC and the PMD AAI. The values from the PMD are lower than those from the MSC. This is not unusual, as different instruments / detectors have their own biases with respect to each other.

For a more in depth assessment about the product quality the reader is referred to the O3MSAF Validation Report on the Aerosol products (document reference ID number: SAF/O3M/KNMI/VR/001).
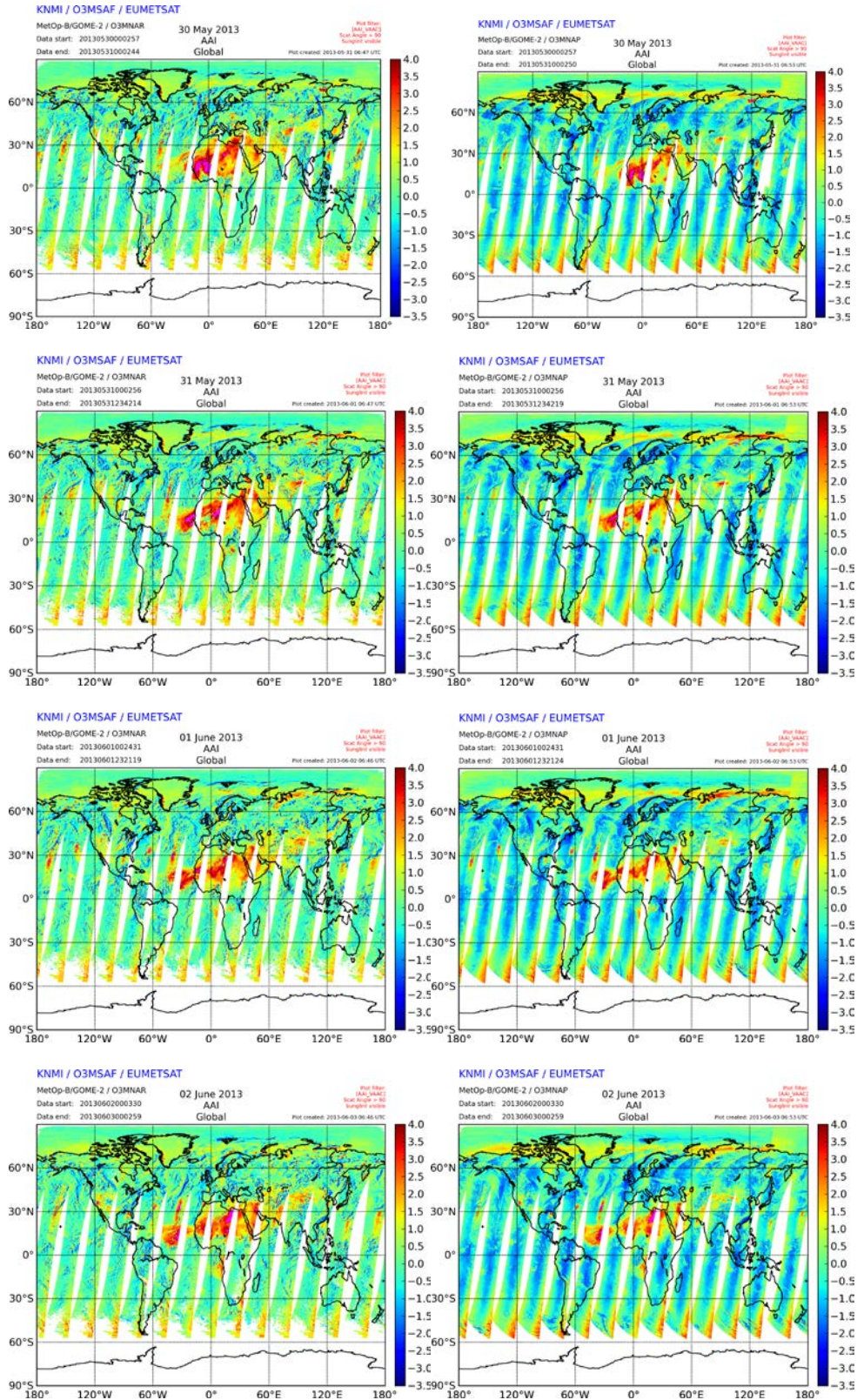
Figure 8: Comparison of AAI from the Main Science Channels (left) against the AAI from the PMD bands (right) from GOME-2 on Metop-B for a desert dust event from 2013-05-30 to 2013-06-02.

7. REFERENCES

Alpert, P., and E. Ganor (2001), Sahara mineral dust measurements from TOMS: Comparison to surface observations over the Middle East for the extreme dust storm, March 14-17, 1998, Journal of Geophysical Research, 106(D16), 18,275-18,286.

Anderson, G. P., S. A. Clough, F. X. Kneizys, J. H. Chetwynd, and E. P. Shettle (1986), AFGL atmospheric constituent profiles, Tech. Rep. AFGL-TR-86-0110, Air Force Geophysics Laboratory.

Chandrasekhar, S. (1960), Radiative Transfer, 393 pp., Dover, Mineola, N.Y. Chiapello, I., J. M. Prospero, J. R. Herman, and N. C. Hsu (1999), Detection of mineral dust over the North Atlantic Ocean and Africa with the Nimbus 7 TOMS, Journal of Geophysical Research, 104(D8), 9277-9291.

de Graaf, M., P. Stammes, O. Torres, and R. B. A. Koelemeijer (2005), Absorbing Aerosol Index: Sensitivity analysis, application to GOME and comparison with TOMS, J. Geophys. Res., 110, D01201, doi:10.1029/2004JD005178

De Haan, J. F., P. B. Bosma, and J. W. Hovenier (1987), The adding method for multiple scattering calculations of polarized light, Astronomy and Astrophysics, 183, 371-391.

Dubovik, O., B. Holben, T. F. Eck, A. Smirnov, Y. J. Kaufman, M. D. King, D. Tanr⊢e, and I. Slutsker (2002), Variability of Absorption and Optical Properties of Key Aerosol Types Observed in Worldwide Locations, Journal of the Atmospheric Sciences, 59, 590-608.

Duncan, B. N., I. Bey, M. Chin, L. J. Mickley, T. D. Fairlie, and R. V. Martin (2003), Indonesian wildfires of 1997: Impact on tropospheric chemistry, Journal of Geophysical Research, 108(D15), D154458, doi:10.1029/2002JD003195.

Gleason, J. F., N. C. Hsu, and O. Torres (1998), Biomass burning smoke measured using backscattered ultraviolet radiation: SCAR-B and Brazilian smoke interannual variability, Journal of Geophysical Research, 103(D24), 31,969-31,978.

Haxby, W. F., J. L. L. G. D. Karner, and J. K. Weissel (1983), Digital images of combined oceanic and continental data sets and their use in tectonic studies, Eos. Trans AUG, 64, 995-1004.

Henyey, L. G., and J. L. Greenstein (1941), Diffuse radiation in the galaxy, Astrophysics Journal, 93, 70-83.

Herman, J. R., P. K. Bhartia, O. Torres, C. Hsu, C. Seftor, and E. A. Celarier (1997), Global distributions of UV-absorbing aerosols from NIMBUS 7/TOMS data, Journal of Geophysical Research, 102(D14), 16,911-16,922.

Hsu, N. C., J. R. Herman, P. K. Bhartia, C. J. Seftor, O. Torres, A. M. Thompson, J. F. Gleason, T. Y. F. Eck, and B. N. Holben (1996), Detection of biomass burning smoke from TOMS measurements, Geophysical Research Letters, 23(7), 745-748.

Hsu, N. C., J. R. Herman, J. F. Gleason, O. Torres, and C. J. Seftor (1999), Satellite Detection of Smoke Aerosols Over A Snow/Ice Surface By TOMS, Geophysical Research Letters, 26(8), 1165-1168.

IPCC (2001), Working Group I to the Third Assessment Report of the Intergovernmental Panel on Climate Change, 295 pp., Cambridge Univ. Press, Cambridge, p. 295.

Koelemeijer, R. B. A., J. F. de Haan, and P. Stammes (2003), A database of spectral surface reflectivity in the range 335-772 nm derived from 5.5 years of GOME observations, Journal of Geophysical Research, 108(D2), D24070, doi:10.1029/2002JD002429.

Mahowald, N. M., and J.-L. Dufresne (2004), Sensitivity of TOMS aerosol index to boundary layer height: Implications for detection of mineral aerosol sources, Geophysical Research Letters, 31, L03103, doi:10.1029/2003GL018865.

Moulin, C., and I. Chiapello (2004), Evidence of the control of summer atmospheric transport of African dust over the Atlantic by Sahel sources from TOMS satellites (1979-2000), Geophysical Research Letters, 31, L02107, doi: 10.1029/2003GL018931.

Pandithurai, G., R. T. Pinker, O. Dubovik, and T. O. Aro (2001), Remote sensing of aerosol optical characteristics in sub-Sahel, West Africa, Journal of Geophysical Research, 106(D22), 28,347-28,356.

Patterson, E. M., D. A. Gillete, and B. H. Stockton (1977), Complex index of refraction between 300 and 700 nm for Saharan aerosol, Journal of Geophysical Research, 82, 3153-3160.

Penning de Vries, M., S. Beirle, T. Wagner (2009), UV Aerosol Indices from SCIAMACHY: Introducing the SCattering Index (SCI), Atmospheric Chemistry and Physics, 9, 9555-9567.

Penning de Vries, M., and T. Wagner (2011), Modelled and measured effects of clouds on UV Aerosol Indices on a local, regional, and global scale, Atmospheric Chemistry and Physics, 11, 12715-12735.

Seftor, C. J., N. C. Hsu, J. R. Herman, P. K. Bhartia, O. Torres, W. I. Rose, D. J. Schneider, and N. Krotkov (1997), Detection of volcanic ash clouds from Nimbus 7/total ozone mapping spectrometer, Journal of Geophysical Research, 102(D14), 16,749-16,759.

Sinyuk, A., O. Torres, and O. Dubovik (2003), Combined use of satellite and surface observations to infer the imaginary part of the refractive index of Saharan dust, Geophysical Research Letters, 30 (D2), 1081, doi:10.1029/2002GL016189.

Stammes, P. (2001), Spectral radiance modelling in the UV-visible range, in IRS 2000: Current problems in atmospheric radiation, edited by W. Smith and Y. Timofeyev, pp. 385-388, A. Deepak Publishing, Hampton (VA).

Tilstra, L.G., M. de Graaf, I. Aben, and P. Stammes (2012a), In-flight degradation correction of SCIAMACHY UV reflectances and Absorbing Aerosol Index, Journal of Geophysical Research, 117, D06209, doi: 10.1029/2011JD016957.

Tilstra, L. G., O. N. E. Tuinder, and P. Stammes (2012b), Introducing a new method for in-flight degradation correction of the Earth reflectance measured by GOME-2, and application to the AAI, in Proceedings of the 2012 EUMETSAT Meteorological Satellite Conference, EUMETSAT P.61, Sopot, Poland.

Torres, O., P. K. Bhartia, J. R. Herman, Z. Ahmad, and J. Gleason (1998), Derivation of aerosol properties from satellite measurements of backscattered ultraviolet radiation: Theoretical basis, Journal of Geophysical Research, 103(D14), 17,099-17,110.

Torres, O., R. Decae, P. Veefkind, and G. de Leeuw (2001), OMI Aerosol Retrieval Algorithm, in OMI-EOS Algorithm Theoretical Basis Document, Chapter 4, pp. 1-24.

Torres, O., P. K. Bhartia, J. R. Herman, A. Sinyuk, P. Ginoux, and B. Holben (2002), A long-term record of aerosol optical depth from TOMS observations and comparison to AERONET measurements, JAS, 59(3), 398-413.

Torricella, F., E. Cattani, M. Cervino, R. Guzzi, and C. Levoni (1999), Retrieval of aerosol properties over the ocean using global ozone monitoring experiment measurements: Method and applications to test cases, JGR, 104(D10), 12,085-12,098.